EES Catalysis

PAPER

View Article Online
View Journal

Cite this: DOI: 10.1039/d6ey00006a

Quantifying buffer transport-limited water electrolysis under non-extreme pH conditions *via* numerical simulations

Melody Wada, Keisuke Obata and Kazuhiro Takanabe *

Received 6th January 2026,
Accepted 24th February 2026

DOI: 10.1039/d6ey00006a

rsc.li/eescatalysis

Water electrolysis carried out under non-extreme pH conditions is expected to play an essential role in a sustainable society as it significantly broadens the choice of materials available for cell components. Buffer species are commonly introduced into electrolytes to minimize local pH gradients through their buffering action; however, the fundamental limitations imposed by buffer transport remain poorly understood. This study focuses on both the hydrogen evolution reaction (HER) and the oxygen evolution reaction (OER) under non-extreme pH conditions. Limiting current densities associated with mass transport of buffer species were quantitatively evaluated. The generalized modified Poisson–Nernst–Planck (GMPNP) model was employed to model achievable mass transport limits of buffer ions and their distribution near the electrode surface. While a buffer's pK_a value affects the limiting current of each half-reaction, consideration of a coupled HER and OER reveals that diffusion of buffer species plays a decisive role in determining the overall performance. Increasing buffer concentration and temperature, assisted by electrolyte convection, effectively enhances the attainable limiting current density beyond industrially relevant thresholds, demonstrating that *electrolyte engineering* through control of buffer chemistry and transport enables buffer-based water electrolysis under non-extreme pH conditions.

Broader context

Water electrolysis is a key technology for large-scale hydrogen production in the transition toward a carbon-neutral society. Current industrial systems predominantly operate in strongly acidic or alkaline electrolytes, which impose constraints on material selection, durability, safety, and system cost. Water electrolysis at non-extreme pH offers an attractive alternative by enabling the use of abundant and corrosion-tolerant materials, improving compatibility with downstream processes, and simplifying system integration. Buffer electrolytes are commonly employed under these conditions to suppress local pH fluctuations near electrode surfaces; however, their suitability for high-current-density operation has remained uncertain, largely due to a lack of quantitative understanding of buffer transport limitations. This work establishes a physics-based framework to clarify how buffer chemistry and mass transport govern the performance of non-extreme pH water electrolysis. By numerically resolving ion transport and reaction coupling for both hydrogen and oxygen evolution, we demonstrate that buffer diffusion limitations at industrially relevant current densities can be systematically mitigated through electrolyte engineering, including optimization of buffer concentration, operating temperature, and electrolyte convection. By providing quantitative design guidance for buffer-based electrolytes, this study expands the feasible operating window for water electrolysis and supports the development of scalable, durable, and material-flexible hydrogen production technologies aligned with long-term sustainability goals.

Introduction

Hydrogen has attracted considerable attention as a vital energy carrier for a carbon-neutral society given its high energy density per mass[1] and the fact that it produces only water upon combustion. Electrochemical water splitting driven by renewable energy resources plays an important role in generating green hydrogen.[2] Current commercial water electrolyzers require corrosion-resistant materials, such as titanium or nickel, for their frame components. This need arises because electrolyzers operate under highly acidic conditions in polymer electrolyte membrane electrolyzers (PEMWEs) or highly alkaline conditions in alkaline water electrolyzers (AWEs).[3–5] These extreme pH conditions are necessary to enhance the ionic conductivities of electrolytes,[6] which minimizes solution resistance and improves energy efficiency.

In recent decades, research has focused on expanding material options *via* water electrolysis in non-extreme pH

Department of Chemical System Engineering, School of Engineering, The University of Tokyo, 7-3-1 Hongo, Bunkyo-ku, Tokyo, 113-8656, Japan.
E-mail: takanabe@chemsys.t.u-tokyo.ac.jp

environments;[7–10] the addition of buffer species to the electrolytes has proven to be important in this regard.[11–15] In terms of the hydrogen evolution reaction (HER), as conditions change from acidic to alkaline, the predominant reduction pathway shifts from proton reduction (reaction (1)) to water-molecule reduction (reaction (2)), although proton reduction is more kinetically favorable.[16,17]

$$2H^+ + 2e^- \rightleftharpoons H_2 \quad (1)$$

$$2H_2O + 2e^- \rightleftharpoons H_2 + 2OH^-. \quad (2)$$

At near-neutral pH values, buffer species influence the kinetics of the HER by enhancing diffusion transport, which necessitates electrolyte engineering to optimize the ion flux.[18] However, the inevitable contribution of ion diffusion slightly decreases HER performance compared with that in extreme pH environments such as a pH of 0.[15]

For instance, HER overpotentials with platinum (Pt), one of the most active catalysts, are primarily due to mass-transport artifacts rather than intrinsic catalytic activity.[11] In buffer solutions containing weak electrolytes (HA), the following reactions occur:

$$HA \underset{k_{ab}}{\overset{k_{af}}{\rightleftharpoons}} H^+ + A^- \quad (3)$$

$$HA + OH^- \underset{k_{bb}}{\overset{k_{bf}}{\rightleftharpoons}} H_2O + A^- \quad (4)$$

where k_{af} and k_{ab} are the forward and backward rate coefficients for buffer protolysis, and k_{bf} and k_{bb} are the forward and backward rate coefficients for basic buffering action. These buffering actions can minimize the local pH fluctuations at the electrode surface,[19,20] which leads to better performance. Some studies have also suggested that buffer species may serve as direct proton donors for the HER,[21,22] as shown by the equation below:

$$2HA + 2e^- \rightleftharpoons H_2 + 2A^- \quad (5)$$

Earlier studies incorporated homogeneous reaction rates into mass-transport equations to quantify the fluxes of various proton sources.[21,22] The results revealed that these reaction rates (eqn (1)) are insufficient to sustain a current density of -10 mA cm^{-2} solely *via* free proton reduction in certain electrolytes.[21,22] The linear free energy relationship between pK_a and k_{af} can be used to estimate the extent of the involvement of free protons as a reactant.[21] Additional experimental evidence has shown that the current–potential behavior of the HER in carbonate buffer with Pt does not display a clear proton limiting current density, unlike in 0.5 M Na_2SO_4.[21] This finding suggests that reactant switching occurs, in which direct carbonate buffer reduction on the surface can predominate at high current densities rather than reactions solely involving free protons.[21,22]

Focusing on the oxygen evolution reaction (OER), which is the other half-reaction of water electrolysis, hydroxide ions are oxidized in alkaline solutions (reaction (6)).[23–25] As solution pH decreases, sufficient hydroxide ions cannot be supplied to the surface, resulting in a local pH shift to more acidic conditions than the bulk pH. When the solution becomes more acidic, the reactant switches to water (reaction (7)).[26–28]

$$4OH^- \rightleftharpoons O_2 + 2H_2O + 4e^- \quad (6)$$

$$2H_2O \rightleftharpoons O_2 + 4H^+ + 4e^- \quad (7)$$

Our group has suggested that hydroxide ions supplied by the basic buffering action (reaction (4)) participate in the reaction by analyzing the Tafel slope, the reaction order, the isotope effect and the temperature sensitivity in various buffer solutions.[14] However, the analysis is limited to current densities below 100 mA cm^{-2}, and it is not clearly understood how many hydroxide ions can be provided by the buffering action. Furthermore, the deprotonated buffer species are considered to help water oxidation, whose reaction can be described by the following.[13]

$$4A^- + 2H_2O \rightleftharpoons O_2 + 4HA + 4e^- \quad (8)$$

Many researchers have studied the OER mechanisms based on hydroxide ion oxidation and water oxidation.[25] Therefore, understanding the reactant in buffer solutions is significant for the fundamental study, which will also provide insights for optimizing the reaction environment to improve OER performance.

The temperature is also elevated[29] as the reaction rate constants increase with temperature according to the Arrhenius expression.[30] At the same time, the lower viscosity and higher conductivity associated with increasing temperature improve mass-transport properties and kinetics.[31] A previous study by our research group examined physicochemical properties (*e.g.*, viscosity and conductivity) of concentrated phosphate buffer solutions at elevated temperatures.[31] Our findings revealed that the experimentally obtained conductivity could be described accurately using the measured viscosity and applying the Stokes–Einstein model, which is typically used for dilute solutions (at least for simple phosphate solutions).[32] Although electrolyte conditions play a very important role in optimizing the performance of water electrolysis, our understanding of how various electrolyte properties affect mass transport of buffer ions remains incomplete.

This study investigated the limiting current density of the HER and OER, which reflects the maximum mass transport of buffer species to the electrode. The mass transport limitation is a prerequisite to water electrolysis regardless of the catalyst kinetics. We simulated the ion distribution in the local environment by considering the fluxes of reactants in electrolyte solutions. To simplify the model, we used Pt as a model catalyst. We numerically solved the migration, diffusion, convection, and homogeneous reactions of electrolytes using the generalized modified Poisson–Nernst–Planck (GMPNP) model, which incorporates the effect of volume exclusion due to ion sizes known as the crowding effect.[33–35] This model is a dilute-solution-based transport model, thus we employed the diffusion coefficients dependent on concentration.

Our simulation results showed that the limiting current density of direct buffer reduction during the HER, $j_{\text{lim-HA red}}$, is further enhanced in solutions with large pK_a values, while the limiting current density of water oxidation supported by buffer species increases in solutions with a small pK_a value. This is derived from the linear free energy relationship of rate coefficients and pK_a in buffering actions. By combining results of the HER and OER, we highlight the importance of diffusion of buffer species from the bulk. Concentration, temperature and convection need to be optimized, which can enhance the limiting current above the industrial requirement. We believe the usage of buffer electrolytes for water electrolysis under non-extreme pH conditions is feasible.

Methodology

Materials

The following chemicals were used for the experiments: $KClO_4$ ($\geq$99.99%, Sigma-Aldrich, Tokyo, Japan), KOH (99.99%, Sigma-Aldrich), $HClO_4$ (70% aqueous solution, FUJIFILM Wako Pure Chemical Corp., Osaka, Japan), $KHCO_3$ (99.7%, Sigma-Aldrich), KH_2PO_4 ($\geq$99.5%, FUJIFILM Wako Pure Chemical Corp.), K_2HPO_4 ($\geq$99.0% after drying at 110 °C, FUJIFILM Wako Pure Chemical Corp.), H_3BO_3 (99.5%, Sigma-Aldrich), $NaClO_4{\cdot}H_2O$ (99.99%, Sigma-Aldrich), NaOH (99.99%, Sigma-Aldrich), $NaHCO_3$ (99.7%, Sigma-Aldrich), $NaH_2PO_4{\cdot}2H_2O$ ($\geq$99.0%, FUJIFILM Wako Pure Chemical Corp.), acetone (Sigma-Aldrich), and isopropanol (FUJIFILM Wako Pure Chemical Corp.). A Pt rotating disk electrode (RDE) and Ni RDE with a diameter of 3 mm were obtained from BAS Inc. (Tokyo, Japan). Pt foil and Pt wire were sourced from Nilaco (Tokyo, Japan). Ultrapure water (18.2 MΩ cm) was used to prepare all of the aqueous solutions.

Electrochemical measurements

We performed electrochemical measurements using either a Pt RDE or Pt foil as the working electrode for the HER experiments. A Ni RDE was utilized for the OER. Prior to each experiment, a Pt RDE was thoroughly polished using a 1-μm diamond suspension and 0.05-μm alumina (BAS Inc.), followed by 5-minute rounds of ultrasonic cleaning in acetone, isopropanol, and ultrapure water. Both the Pt RDE and Pt foil were cleaned electrochemically using cyclic voltammetry (CV) in 1 M $HClO_4$ with cycling between approximately −0.05 V and 1.85 V *versus* the standard hydrogen electrode (SHE) with argon bubbling ($\geq$99.9999%). A Ni RDE was polished and sonicated without any electrochemical cleaning. Ag/AgCl electrodes (saturated KCl, BAS Inc.) were used as reference electrodes, and Pt wire was used as the counter electrode in all experiments.

For the buffer solutions, the buffer species were dissolved to achieve a concentration of x M, and the pH was adjusted to obtain particular pK_a values. To prepare 100 mL of x M carbonate at pH 10.3, a stoichiometric amount of salts was dissolved in approximately 80 mL of water, followed by pH and volume adjustments using concentrated KOH or NaOH solutions and additional water. Similarly, for x M phosphate at pH 7.2, x M MH_2PO_4 (M = K or Na) was dissolved in about 80 mL of water, followed by the corresponding pH and volume adjustments.

During all of the measurements, we continuously supplied H_2 gas ($\geq$99.99999%) or O_2 gas (99.99995%) to the electrochemical cell for the HER or OER experiments, respectively. Experiments using Pt foil were conducted under stationary conditions (*i.e.*, without rotation). We used CV and potentiostatic electrochemical impedance spectroscopy (PEIS) with a 16-channel research-grade potentiostat system (VMP3, BioLogic Science Instruments, Grenoble, France). The electrolyte temperature was managed by immersing the electrochemical cell in a water bath or using a water-jacketed glass cell (BAS Inc.) with an external temperature control system (NCB-1210, Eyela, Tokyo, Japan). All current densities are reported relative to the geometric electrode surface area. *iR* correction was performed using impedance values measured at frequencies of at least 100 kHz with an amplitude of 10 mV.

Electrochemical modeling

One-dimensional simulations were conducted using the GMPNP model. As illustrated in Fig. S3, the mass-transport region in front of the electrode consists of three distinct layers: the Stern layer, the diffuse layer, and the diffusion layer. The outer Helmholtz plane (OHP) coincides with the centers of the ions nearest the electrode surface, which form the Stern layer.[33,36] The diffuse layer is characterized by a departure from electroneutrality as cations are attracted to the negatively charged cathode while anions are repelled during the HER.[37] Together, the Stern and diffuse layers form the electrical double layer (EDL). Further from the electrode, the diffusion layer maintains electroneutrality, and mass transport is governed primarily by diffusion and convection. Species transport was modeled by starting from the OHP; the ion distribution and electrostatic potential were described using the GMPNP model.

Mathematical framework. At steady state, the species mass-transport in the electrolyte can be defined in the following equation.

$$\frac{\partial c_i}{\partial t} = -\nabla J_i + R_i = 0 \tag{9}$$

where c_i, J_i, and R_i are the concentration, the flux, and the homogeneous chemical reaction rate of species i, respectively. t expresses time. In the GMPNP model, the Nernst-Planck equation uses the species flux J_i described as:

$$J_i = -D_i\nabla c_i + vc_i - \frac{D_i c_i z_i F}{RT}\nabla\phi - D_i c_i\left(\frac{N_A\sum_{i=1}^{n} A_i^3\nabla c_i}{1 - N_A\sum_{i=1}^{n} A_i^3 c_i}\right) \tag{10}$$

where D_i, z_i, and A_i are the diffusion coefficient, the charge number, and the thermochemical size of species i, respectively.

v, F, R, T, ϕ, and N_A are the fluid velocity at a distance x from the OHP, the Faraday's constant, the gas constant, the temperature, the electrostatic potential, and the Avogadro's number, respectively. Each term accounts for diffusion, convection, migration and steric exclusion due to ion sizes. Close to the surface of RDE, the velocity of the fluid v depends on the rotation speed and electrolyte properties:[30]

$$v = \left(\omega\frac{\eta}{\rho}\right)^{\frac{1}{2}}\left[-0.510\left(\frac{\omega\rho}{\eta}\right)x^2 + 0.333\left(\frac{\omega\rho}{\eta}\right)^{\frac{3}{2}}x^3 - 0.103\left(\frac{\omega\rho}{\eta}\right)^{2}x^4\right] \quad (11)$$

where ω, η and ρ are the angular velocity, dynamic viscosity and density, respectively. The Poisson equation connects the relationship between ion distributions and the electrostatic potential:

$$\nabla(\varepsilon_0\varepsilon_r\nabla\phi) = -F\sum_{i=1}^{n} z_i c_i \quad (12)$$

where ε_0 and ε_r are the permittivity of vacuum and the relative permittivity of water, respectively. In this model, ε_r was assumed to be constant regardless of the conditions.

Homogeneous reactions. The homogeneous reactions in eqn (9) include self-ionization of water and buffering actions. Self-ionization of water is a chemical process in which water molecules are dissociated into protons and hydroxide ions.

$$H_2O \underset{k_{wb}}{\overset{k_{wf}}{\rightleftharpoons}} H^+ + OH^- \quad (13)$$

where k_{wf} and k_{wb} are the forward and backward rate coefficients, respectively. The equilibrium coefficient of this reaction is:

$$K = \frac{a_{H^+}a_{OH^-}}{a_{H_2O}} \quad (14)$$

where a_i is the activity of species i. Because the activity of solvent water is assumed to be 1 in diluted solutions, the water ionization coefficient is conventionally reported as:[38]

$$K_w = a_{H^+}a_{OH^-} \quad (15)$$

While a_{H_2O} can decrease in concentrated electrolyte, this model treated a_{H_2O} as 1 regardless of the electrolyte conditions for simplicity. The activity of species i is defined as

$$a_i = \gamma_i\frac{c_i}{c^\circ} \quad (16)$$

where γ_i and c° are the activity coefficient of species i and the standard concentration (1 M), respectively. This study assumes γ_H and γ_{OH} were equal to 1. Then, eqn (14) and (15) can be connected with units.

$$K = K_w = \frac{c_{H^+}c_{OH^-}}{c_{H_2O}}[\text{mol L}^{-1}] \quad (17)$$

where c_{H_2O} is 1 M. The temperature dependence of K_w is reported.

Buffering actions are described in Reactions (3) and (4). Single-ion activity coefficients are difficult to measure in solutions, so the mean activity coefficient γ is often used. Using γ, the equilibrium coefficients can be described as follows:

$$K_a = \frac{a_{H^+}a_{A^-}}{a_{HA}} = \frac{(c_{H^+}/c^\circ)(\gamma c_{A^-}/c^\circ)}{(\gamma c_{HA}/c^\circ)} = \frac{(c_{H^+}/c^\circ)(c_{A^-}/c^\circ)}{(c_{HA}/c^\circ)} \quad (18)$$

$$K_b = \frac{a_{H_2O}a_{A^-}}{a_{HA}a_{OH^-}} = \frac{(c_{A^-}/c^\circ)}{(c_{HA}/c^\circ)(c_{OH^-}/c^\circ)} = \frac{K_a}{K_w}. \quad (19)$$

These equilibrium coefficients can also have units of:

$$K_a = \frac{k_{af}}{k_{ab}} = \frac{c_{H^+}c_{A^-}}{c_{HA}}\ [\text{mol L}^{-1}] \quad (20)$$

$$K_b = \frac{k_{bf}}{k_{bb}} = \frac{c_{H_2O}c_{A^-}}{c_{HA}c_{OH^-}}[-]. \quad (21)$$

In summary, R_i of each species becomes:

$$R_{H^+} = k_{wf}c_{H_2O} - k_{wb}c_{H^+}c_{OH^-} + k_{af}c_{HA} - k_{ab}c_{H^+}c_{A^-} \quad (22)$$

$$R_{OH^-} = k_{wf}c_{H_2O} - k_{wb}c_{H^+}c_{OH^-} - k_{bf}c_{HA}c_{OH^-} + k_{bb}c_{H_2O}c_{A^-} \quad (23)$$

$$R_{HA} = -k_{af}c_{HA} + k_{ab}c_{H^+}c_{A^-} - k_{bf}c_{HA}c_{OH^-} + k_{bb}c_{H_2O}c_{A^-} \quad (24)$$

$$R_{A^-} = k_{af}c_{HA} - k_{ab}c_{H^+}c_{A^-} + k_{bf}c_{HA}c_{OH^-} - k_{bb}c_{H_2O}c_{A^-}. \quad (25)$$

The forward rate coefficient of buffer protolysis (k_{af}) from eqn (3) and the backward rate coefficient of basic buffering action (k_{bb}) from eqn (4) were obtained from previously reported values[33,39,40] or estimated using the linear free energy relationship with the buffer species' K_a values as reported in previous studies.[14,21]

$$\log k_{af} = 0.99\log K_a + 11 \quad (26)$$

$$\log k_{bb} = -1.2\log K_a - 6.7 \quad (27)$$

We considered k_{af}, k_{bb}, and k_{wf} to be irrelevant to the temperature, which led to changes of k_{ab}, k_{bf}, and k_{wb} occurring with changes in K_a, K_b, and K_w.

Boundary conditions for species concentration: When the catalyst reaction is fast enough, the current density is determined by the surface flux of the reactant species. Once the reactant comes to the surface, it is consumed and the resultant surface concentration becomes zero. To simulate the limiting current densities of direct HA reduction, both the proton and HA concentrations at the OHP were set to zero. The fluxes of non-reactive species were also set to zero:

$$c_{H^+,HA} = 0 \quad (28)$$

$$J_{OH^-} = 0 \quad (29)$$

$$J_{HA} + J_{A^-} = 0 \quad (30)$$

$$j_{\text{lim-HA red.}} = F(J_{H^+} + J_{HA}) \quad (31)$$

H_3PO_4 and $H_2PO_4^-$ were consumed in phosphate, while H_2CO_3 and HCO_3^- were consumed in carbonate.

For the OER, the limiting current densities of hydroxide ion oxidation, $j_{\text{lim-OH oxi}}$, was defined by the surface flux of hydroxide ions, and the concentration of hydroxide ions at

the OHP was set to zero. Fluxes of the other species were set to zero.

$$C_{OH^-} = 0 \quad (32)$$

$$J_{H^+,HA,A^-,K^+} = 0. \quad (33)$$

$$j_{lim\text{-}OH\ oxi.} = -FJ_{OH^-} \quad (34)$$

The limiting current densities for water oxidation helped by deprotonated buffer species, $j_{lim\text{-}A\ oxi.}$ were defined by the surface fluxes of hydroxide ions and deprotonated buffer species. The concentrations of hydroxide ions and deprotonated buffer species at the OHP were set to zero. Conservation of buffer species must be satisfied (eqn (38)).

$$C_{OH^-,A^-} = 0 \quad (35)$$

$$J_{H^+,K^+} = 0 \quad (36)$$

$$J_{HA} + J_{A^-} = 0 \quad (37)$$

$$j_{lim\text{-}A\ oxi.} = -F(J_{OH^-} + J_{A^-}). \quad (38)$$

The bulk electrolyte obeys electroneutrality:

$$\sum_{i=1}^{n} z_i c_i = 0 \quad (39)$$

The bulk concentrations of species were determined using the buffer's equilibrium equations and the electroneutrality. For a 3 M K-buffer solution, the total buffer concentration was set to 3 M. A list of example values is provided in Table S6.

Boundary conditions for charge. Boundary conditions for charge at the OHP were determined using the capacitance of the Stern layer:

$$\varepsilon_0\varepsilon_r\nabla\phi|_{x=0} = C_{Stern}(\phi_{OHP} - \phi_M) \quad (40)$$

where C_{Stern}, ϕ_{OHP}, and ϕ_M are the Stern layer capacitance, the potential at the OHP and the potential of the electrode, respectively. This study assumed the C_{Stern} value to be 20 μF cm^{-2} as previously reported in the field of electrochemical CO_2 reduction,[37] which is consistent with earlier studies investigating the EDL.[41,42] The applied potential ϕ_M was adjusted to −0.2 V or 1.5 V *versus* a reversible hydrogen electrode (RHE) or otherwise noted, including the solution resistance, R_{sol}:

$$\begin{aligned}\phi_M &= -0.2(1.5) + j_{lim}R_{sol} + \frac{RT\ln 10}{F}\text{pH} \\ &= -0.2(1.5) + \frac{j_{lim}L}{\sigma} + \frac{RT\ln 10}{F}\text{pH [V } \textit{vs.}\text{ SHE]}\end{aligned} \quad (41)$$

where L is the calculated length (500 μm in this study) and SHE is the standard hydrogen electrode. σ is the conductivity of the electrolyte:

$$\sigma = \frac{F^2}{RT}\sum_{i=1}^{n} z_i^2 c_i D_i \quad (42)$$

The RHE serves as a theoretical reference electrode in reaction (1), and its potential is defined to be 0 V at all temperatures.[30] The bulk potential was set to be 0 V *versus* the potential at the point of zero charge (PZC), where the net electrode surface charge is zero. The PZC of Pt has been estimated to be 0.23 V *versus* SHE at room temperature[43] and assumed to be irrelevant to temperature.

Parameters. We measured the dynamic viscosity (η) and density (ρ) of the electrolytes using an Anton Paar SVM 2001viscometer, as shown in Fig. S6. The diffusion coefficients D_i under the specified electrolyte conditions were estimated[15,31] using the Stokes–Einstein equation based on the diffusion coefficients at infinite dilution, D_{i0}:[38]

$$D_i = \frac{kT}{6\pi r\eta} = D_{i0}\frac{\eta_0}{\eta}\frac{T}{T_0} \quad (43)$$

where k, r, η_0 and T_0 are the Boltzmann constant, the effective hydrodynamic radius of the hydrated ion (the Stokes radius), the dynamic viscosity of water and the standard temperature (in this case 25 °C) respectively. Complete lists of the parameters used are provided in the SI.

Numerical methods. COMSOL Multiphysics solved two domain equations (*i.e.*, Nernst–Planck and Poisson equations) concurrently using two general form PDE modules. The modeling domain was divided into six regions: 0–1 nm, 1–10 nm, 10–100 nm, 100 nm–1 μm, 1–150 μm, and 150–500 μm. The corresponding maximum element sizes for meshing were set as follows: 5×10^{-3} nm (for 0–1 nm), 1×10^{-2} nm (for 1–10 nm), 5×10^{-2} nm (for 10–100 nm), 0.5 nm (for 100 nm–1 μm), 5 nm (for 1–150 μm), and 0.1 μm (for 150–500 μm). This meshing strategy resulted in a total of 41 009 elements. Finer mesh in 1–10 nm (5×10^{-3} nm) changed the resultant limiting current density within 0.1%, indicating the sufficient fineness. A relative solver tolerance for species concentration and potential was 0.001, which ensures accuracy but curbs the computational cost.

Results and discussion

Experimental behaviors in the HER and OER

The contribution of buffer species to electrolytes under non-extreme pH conditions to improve water electrolysis primarily involves suppressing local pH shifts and directly participating in catalytic reactions. Thus, it is important to understand how buffer species influence the limiting current density of the HER and OER to optimize their performance.

Fig. 1(a) shows the current–voltage behaviors in the HER measured with a Pt RDE in 25 mM K-buffer electrolytes with different rotation speeds, which illustrate the experimental observations of $j_{lim\text{-}HA\ red}$. The pH values were adjusted near their respective pK_a values at room temperature (carbonate: pK_a 10.3, borate: pK_a 9.2, phosphate: pK_a 7.2 or 12.3)[38] to maintain an optimal balance between protonated and deprotonated species for effective pH stabilization. An RDE was used to precisely control the diffusion layer thickness. During the measurements, hydrogen gas flowed into the cell, and the equilibrium potentials of the HER and hydrogen oxidation reaction (HOR) were defined as the potentials at which the current was zero and set at 0 V *versus* RHE.

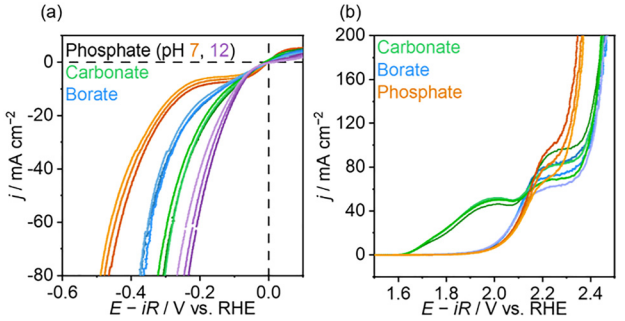

Fig. 1 Experimentally measured cyclic voltammograms at room temperature and a scan rate of 200 mV s^{-1}. Electrolyte pH values were adjusted to near the buffer's pK_a value. (a) Positive scan measured in 25 mM K-buffer electrolyte. Supporting salt of 0.1 M $KClO_4$ was added. Pt rotating disk electrode was rotated at 2500, 3600 or 4900 rpm under a H_2 flow. (b) Negative scan measured in 0.1 M Na-buffer electrolyte. Supporting salt of 1 M $NaClO_4$ was added. A Ni rotating disk electrode was rotated at 2500, 3600 or 4900 rpm under O_2 flow.

We observed three-step cathodic current behavior in the phosphate electrolyte. The current magnitude initially increased with increasing overpotential and reached a plateau at approximately -7 mA cm^{-2} before increasing further. As the rotation speed decreased, the plateau current shifted to less negative values, which clearly indicates this plateau derives from the mass transport of buffer species. Of note, a previous study measured CVs in 0.5 M Na_2SO_4 at various pH values on Pt RDE and any limiting current density was observed at pH $>$ 5.[44] Conversely, no apparent limiting current was observed in borate and carbonate; a steady increase in current magnitude is realistic given that water reduction is feasible over this pH range. Fig. S1(a) added the experimental behavior at different temperatures. The plateau observed in phosphate at pH 7 shifted negatively at high temperatures.

Due to the difficulty of applying high current densities ($>$100 mA cm^{-2}) on RDEs, a platinum foil electrode without rotation was used with varying concentrations of K-phosphate buffer (Fig. S2(b)). The current plateaued around -0.55 mA cm^{-2} in 25 mM K-phosphate, which shifted negatively to around -43 mA cm^{-2} in 0.5 M K-phosphate. Fig. S2(c) shows the differentiate current density as a function of potential. With increasing concentration, the plateau current's boundary became less distinct. At higher current magnitudes, bubble formation likely induced electrolyte circulation within the cell, which reduced the diffusion layer thickness.[45] Observing the limiting current experimentally is challenging; we accordingly turned to numerical simulations to quantify the dependence of $j_{\text{lim-HA red}}$ on various electrolyte properties.

Similar experiments were conducted for the OER. The CVs were measured using a Ni RDE in 0.1 M Na-buffer solutions with 1 M $NaClO_4$. $NaClO_4$ was added into solutions to increase the ionic conductivity. The pH values of electrolytes were adjusted near the buffers' respective pK_a values at room temperature. Ni is a commonly used material for the OER.[46] Before and during all measurements, oxygen gas was saturated in the cell. As shown in Fig. 1(b), three-step anodic current behavior was observed in all electrolytes. The current density increased as the overpotential increased, followed by plateaus, and sharply increased again. Of note, a previous study conducted CVs in 0.1 M Na-phosphate at pH 7 on IrO_x and a plateau occurred in a similar current region.[14] Since these plateaus were affected by the rotation speed of RDE, current densities in this region are affected by the mass transport of species. We have to note that, because noticeable current was not observed during water oxidation in unbuffered solution at pH 7 or 9 and in a similar potential range,[28] participation of buffer ions at the reaction interface should play an important role.

Notably, a lower OER onset potential was observed in carbonate. While the onset potential was similar to that in other buffer electrolytes in the first cycle, the oxidation current increased and the onset potential shifted with increasing cycle numbers (Fig. S2). This is probably because iron impurities contained in carbonate salts were deposited on Ni, leading to higher OER performance. Since the plateau region between 1.5 and 1.7 V *vs.* SHE was dependent to the rotation speed but not to measurement cycles, we considered this region to be mainly affected by the mass transport of species.

Modeling of the limiting current density of direct buffer reduction in specific buffer electrolytes

The dependency of the limiting current of direct buffer reduction, $j_{\text{lim-HA red.}}$ on the buffer-ion concentrations was quantitatively assessed using numerical simulations. Eqn (9) and (10) were used to model species mass transport in terms of concentration, despite our previous findings suggesting that activity provides a more accurate representation.[15] We considered thermochemical ion sizes in the steric term since the solvated sizes were too large to take into account the crowding effect and could no longer be sustained in concentrated buffer electrolytes. Additional details regarding the impact of activity coefficients and thermochemical ion sizes are provided in the SI.

Fig. 2(a) shows the simulated $j_{\text{lim-HA red.}}$ in K-phosphate and K-carbonate electrolytes; we assumed that the pH values

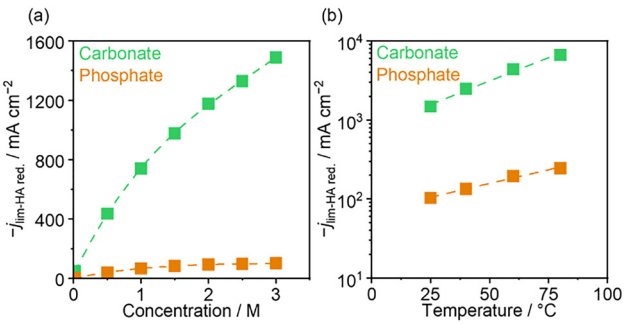

Fig. 2 (a) Concentration dependence of the calculated limiting current density of direct buffer reduction to H_2, $j_{\text{lim-HA red.}}$. All of the electrolytes were assumed to have a pH value the same as the pK_a value. A supporting electrolyte of 0.1 M $KClO_4$ was considered as an addition to the 25 mM K-buffer electrolytes. Pt rotating disk electrodes were assumed to rotate at 100 rpm at 25 °C. The dotted lines are fit lines based on cubic functions. (b) Simulated temperature dependence of $j_{\text{lim-HA red.}}$ in 3 M K-buffer electrolytes. The dotted lines are fit lines.

matched their respective pK_a values of 7.20 and 10.33. In K-phosphate, increasing the concentration from 0.025 M to 3 M led to an increase in $-j_{\text{lim-HA red.}}$ from 2.5 to 102 mA cm^{-2}. This increase was not linear with respect to concentration, because the increased viscosity (Fig. S7) led to decreases in the diffusion coefficients. In our previous study, conductivity was calculated using the Stokes–Einstein equation from measured viscosity and showed quantitative agreement with experimental values.[31] Therefore, the model likely remains valid under these conditions.

Notably, the thickness of the diffusion layer on a Pt foil electrode under experimental conditions was assumed to be similar to that of a Pt RDE at 100 rpm, as indicated by the rotation-dependent data shown in Fig. S9. The simulated $-j_{\text{lim-HA red.}}$ accurately reproduced the experimental results. Compared with phosphate, a greater increase in $-j_{\text{lim-HA red}}$ was observed in the K-carbonate buffer; at the same concentration, $-j_{\text{lim-HA red.}}$ was larger in K-carbonate than in K-phosphate. The simulation showed that $-j_{\text{lim-HA red.}}$ reached 1489 mA cm^{-2} in 3 M K-carbonate, which is over 14 times greater than the result obtained in 3 M K-phosphate.

We also investigated the impact of temperature on $j_{\text{lim-HA red}}$. Simulated $j_{\text{lim-HA red.}}$ in 3 M K-buffer electrolytes at elevated temperatures are described in Fig. 2(b). Notably, changes occurred in the concentration determined by molarity (M) according to temperature as the volume of the electrolytes changed. Fig. S8 shows the molarity at different temperatures obtained from experimentally measured densities and the relationship between molarity and molality (m). The difference in molarity according to temperature was small, so we considered the molarity to be constant at all temperatures in this model. The pH of the electrolytes was assumed to match the pK_a values of the buffer ions at these temperatures. It is important to note that the pH values of commercial pH standard electrolytes shift in accordance with the pK_a at elevated temperatures. Fig. S10(b) summarizes the pK_a and pK_w values with respect to temperature based on previously reported values.[38] Interestingly, pK_w is particularly sensitive to temperature changes, whereas the pK_a values of phosphate and carbonate are not significantly affected. The temperature dependence of the equilibrium coefficients was characterized using enthalpy and heat capacity (see the SI for detailed calculation methods) (Table S1). About the rate coefficients of homogeneous reactions, k_{af}, k_{bb}, and k_{wf} were assumed to be independent of temperature and k_{ab}, k_{bf}, and k_{wb} were changed correspondingly as it is difficult to define the activation energy of those reactions. The impact of this assumption is discussed in the SI.

As illustrated in Fig. 4(c), $j_{\text{lim-HA red.}}$ in 3 M K-phosphate was 2.4 times higher at 80 °C than at 25 °C. This increase is reasonable given that a decrease in viscosity typically leads to higher diffusion coefficients (Fig. S10). On the other hand, $j_{\text{lim-HA red}}$ was more than four times higher at 80 °C than at 25 °C in K-carbonate. This significant increase cannot be attributed solely to a decrease in viscosity.

Modeling of the limiting current density of direct buffer reduction in buffer electrolytes

We focused on the distinct chemical properties of phosphate and carbonate buffers to explain their different limiting current behaviors. Apart from ion concentrations and temperatures, significant distinctions at various temperatures include the electrolyte pH, pK_a of the buffer species, and pK_w of water. For simplicity, we considered a single-step buffer equilibrium (HA^-/A^{2-}) rather than specific buffer species. The protonated buffer molecule was assumed to be negatively charged, which is consistent with the charges of $H_2PO_4^-$ and HCO_3^-. Charge effects are summarized in the SI.

We first simulated the limiting current density for the direct reduction of HA^- to A^{2-} across various pH values spanning from neutral to alkaline conditions to examine pH dependence (Fig. S12(a)). The conditions included 3 M $K_{1.5}H_{0.5}A$ buffer electrolytes with pK_a values ranging from 7 to 10. We varied the ratio of buffer species according to the electrolyte pH and maintained a total buffer species concentration of 3 M. The forward rate coefficient of buffer protolysis (k_{af}) from reaction (3) and the backward rate coefficient of basic buffering action (k_{bb}) from reaction (4) were estimated using the buffer species' K_a (eqn (26) and (27)). We adjusted parameters such as viscosity, diffusion coefficients, and ion sizes from K-carbonate values to ensure data comparability. The simulated $-j_{\text{lim-HA red.}}$ value in buffer solutions with a pK_a of 7 was -173 mA cm^{-2} at pH 7, which is similar to the result obtained in 3 M K-phosphate at pH 7.2. This value decreased with increasing solution pH. $-j_{\text{lim-HA red}}$ values in buffer solutions with larger pK_a values were significantly larger at the same pH. This difference arises from the decreased concentration of protonated buffer species in the bulk as the pH exceeds the pK_a of the buffer species, as shown in Fig. S12(b). Therefore, pH may not be the primary factor contributing to the differences between phosphate and carbonate.

A quantitative analysis of the pK_a dependence was also conducted using a single-step buffer equilibrium while varying pK_a. The buffer electrolytes were 3 M $K_{1.5}H_{0.5}A$; pH values corresponded to pK_a values. The simulated $j_{\text{lim-HA red.}}$ is illustrated in Fig. 3(a). This figure shows that there was a significant increase in $-j_{\text{lim-HA red}}$ as the buffer pK_a increased. Fig. 3(b) shows the local concentration profiles of protonated buffer species at 25 °C as a function of distance from the electrode surface. The inset figure is a magnified version focusing on the diffuse layer. In 3 M solutions with a pK_a of 7, the concentration steadily decreased toward the electrode, and there was full depletion at the surface. As in K-phosphate, $j_{\text{lim-HA red.}}$ was governed by the diffusion of protonated buffer species when the pK_a was low. On the other hand, three phases in the buffer with pK_a 12 were observed: a steep decline in concentration from 150 to 100 μm, followed by an approximate plateau at 0.35 mM until 1 nm, and then a sharp drop at the surface. A larger concentration of protonated buffer species in the diffuse layer results in a higher obtainable current density in the buffer with pK_a 12. Buffer species with larger pK_a values have a larger

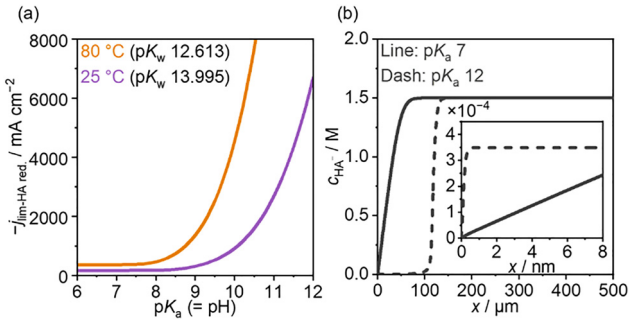

Fig. 3 (a) Calculated limiting current density of direct buffer reduction. We assumed that the buffer was 3 M $K_{1.5}H_{0.5}A$, which means that the pH value was equal to the pK_a value. The Pt rotating disk electrode was assumed to rotate at 100 rpm. The dotted lines are the fit lines. (b) The simulated concentration profile of the protonated buffer species in the solutions as a function of distance from the electrode surface in 3 M buffer electrolytes. The inset figure shows the concentration profiles in the diffuse layer.

backward rate coefficient in reaction (4) thanks to the linear free relationships as reported in a previous study.[21] Thus, deprotonated buffer species can easily be converted to protonated buffer species in solutions with a pK_a of 12, leading to a higher concentration at the surface than that in solutions with a pK_a of 7. As a result, the surface flux of protonated buffer species is enhanced.

At 80 °C, $-j_{\text{lim-HA red}}$ was larger even at the same pK_a (Fig. 3(a)). The viscosity and density parameters of K-carbonate at 80 °C were used. As noted above, higher temperatures increase water dissociation, which results in a pK_w of 12.6 at 80 °C, and the rate coefficients of buffering actions were determined using eqn (26) and (27) irrespective of temperature. Considering the reduction of viscosity at high temperature (Fig. S10), the main cause of the increase in $-j_{\text{lim-HA red}}$ with temperature can be attributed mainly to the pK_w. Acceleration of water dissociation makes the basic buffering action (reaction (4)) occur more easily. Previous studies have shown that when two buffer species with similar pK_a values are combined, the maximum buffer capacity occurs at a pH between their intrinsic pK_a values.[47] In this framework, the self-ionization of water can act as a buffer with a pK_a of 13.995 at 25 °C or 12.613 at 80 °C. Similarly, as a buffer's pK_a nears pK_w, the self-ionization of water can offer additional proton donors, which increases the buffer capacity, even under alkaline conditions.

Using the proton limiting current densities calculated with previously reported methods,[48] Fig. S13 summarizes the reaction during the HER in 3 M K-buffer electrolyte where pH = pK_a. Under extremely acidic pH conditions (*i.e.*, pH < 1), free proton reduction is possible until a high current density. As buffer pH (pK_a) increases, protons can be supplied *via* buffer protolysis. Even so, a current density above approximately 170 mA cm^{-2} should be attained only with direct water reduction at 25 °C. Direct reduction of protonated buffer species becomes effective in buffer with pK_a > 5, which is enhanced as pK_a increases thanks to reaction (4). At high temperature, the limiting current can be further enhanced.

Modeling of the limiting current density of the OER in buffer electrolytes

To clarify the plausible reactant during the OER, the simulation was conducted while varying the boundary conditions considering reaction (6) and (8). For simplicity, single-step buffering action (HA^-/A^{2-}) was considered and deprotonated buffer species, A^{2-} were assumed to be divalent anions similar to carbonate (HCO_3^-/CO_3^{2-}) and phosphate ($H_2PO_4^-/HPO_4^{2-}$) cases. The pH of the buffer electrolytes was fixed at the buffers' pK_a. Parameters such as viscosity and density were taken from values measured in 3 M K-carbonate. Fig. 4 shows the simulated limiting current density of hydroxide ion oxidation, $j_{\text{lim-OH oxi.}}$ in 3 M K-buffer electrolytes. At pH > 13, $j_{\text{lim-OH oxi.}}$ increases since the alkaline condition increases hydroxide concentrations. For pK_a values from 10 to 13, $j_{\text{lim-OH oxi.}}$ was almost independent of electrolyte pH or the buffer's pK_a, which suggests that the diffusion of buffer species purely determined the obtainable current density. The rate of the backward reaction of reaction (4) might be fast enough to supply hydroxide ions close to the electrode due to the linear free relationship with pK_a.[14]

On the other hand, $j_{\text{lim-OH oxi.}}$ decreases below pK_a 10. This is due to the slow rate of the backward reaction in reaction (4). Considering that the plateau current measured in the phosphate solution at pH 7 (Fig. 1(b)) was at a similar level with those in carbonate and borate solutions, the plateau current is not likely determined by hydroxide ion oxidation solely. In the phosphate solution at pH 7, the reactant switching may occur before the current reaches a plateau.

Therefore, the limiting current of water oxidation supported by deprotonated buffer species (reaction (5)) was considered. As shown in Fig. 4, above pK_a 10, the limiting current of water oxidation supported by buffer species (purple line), $j_{\text{lim-A oxi.}}$ is identical to that of hydroxide ion oxidation (blue line). Because of the facile backward reaction in reaction (4) in this pK_a range, they cannot be distinguished just from the limiting current density. Between pK_a 8 and 10, $j_{\text{lim-A oxi.}}$ remains almost constant, indicating that the experimentally observed limiting

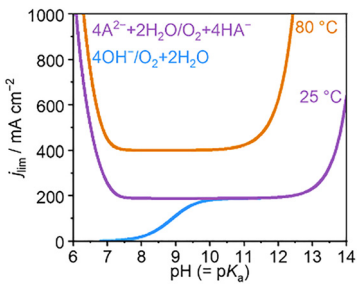

Fig. 4 The limiting current density of hydroxide ion oxidation (reaction (6)) and water oxidation supported by deprotonated buffer species (reaction (8)) during the OER in 3 M K-buffer (HA^-/A^{2-}) solutions. Electrolyte pH values were assumed to be the same as the buffer's pK_a values. Ni RDE was assumed to rotate at 100 rpm. Properties such as electrolyte viscosity, density, diffusion coefficients, and ion sizes were taken from 3 M K-carbonate solutions.

current shown in Fig. 1(b) might just reflect the mass transport limitation of deprotonated buffer species regardless of the reactant (hydroxide ions or water molecules). Because the experimentally obtained limiting current density in a borate solution at pH 9 and a phosphate solution at pH 7 are larger than those coming from hydroxide ion oxidation, the anodic reaction may have shifted to water oxidation supported by buffer ions.

$j_{\text{lim-A oxi.}}$ increases at pK_a < 8. $j_{\text{lim-A oxi.}}$ at pK_a 8 is 189 mA cm^{-2}, reaching 1156 mA cm^{-2} at pK_a 6. Fig. S14 describes concentration of deprotonated buffer species as a function of distance from the OHP at the limiting current density. In buffer solutions with pK_a 10, the concentration profile of deprotonated buffer species clearly matches the diffusion limited profile. It starts to decrease from around 70 μm to the depletion at x = 0. In solutions with pK_a 6, on the other hand, the usage of deprotonated buffer species starts earlier (90 μm) and the concentration profile reaches a plateau. Buffer species with smaller pK_a values have larger forward rate coefficients thanks to the linear free relationships as reported in a previous study.[21] Thus, protonated buffer species can easily be converted to deprotonated buffer species in solutions with a pK_a of 6, leading to a higher concentration at the surface than that in solutions with a pK_a of 10. As a result, the surface flux of deprotonated buffer species is enhanced.

The limiting current was also simulated at the elevated temperature of 80 °C (orange line in Fig. 4). When temperatures increase, the viscosity of the electrolyte decreases, making diffusion coefficients larger following the Stokes–Einstein equation, as shown in Fig. S10(a). The enhancement of $j_{\text{lim-A oxi.}}$ at pK_a < 10 is reasonable. At a pK_a > 10, further enhancement is observed. The log scale of water ionization constant, pK_w decreases thermodynamically according to temperature changes, thus, the amount of hydroxide ions in the solution is greater even at the same pH, resulting in an enhancement of the limiting current of the OER.

Combination of the HER and OER

Combining results of the HER and OER, the achievable current densities in the presence of buffer are summarized in Fig. 5. Of note, the combined limiting current densities can be obtained when two decoupled or distant half-cells operate. The conditions are 3 M K-buffer solutions containing ion pairs of HA^-/A^{2-} at 100 rpm, with the pH set equal to the buffer's pK_a. When the pK_a is small (<8), the limiting current for the OER side (the data is from Fig. 4) increases, but the HER cannot be helped beyond the diffusion of buffer species from the bulk. Similarly, the limiting current for the HER side (the data is from Fig. 3) increases in buffer solutions with large pK_a values (>8), and the limitation occurs at the OER side. The limiting current of the HER and OER crosses around pK_a 8, where both the HER and OER are simply limited by the diffusion of buffer species from the bulk.

Elevated temperature enhances the limiting current, while the achievable current densities of these reactions remain < 400 mA cm^{-2}, which is not sufficient in terms of the industrialization requiring 600 mA cm^{-2}. Therefore, it is necessary to improve the diffusion of buffer species to enhance the performance of water electrolysis under non-extreme pH conditions. While optimizing the species charge was suggested in previous studies,[49,50] the OER and HER are incompatible. For the HER, positively charged buffer species are preferable since the cathode is negatively charged, and the OER favors negatively charged species. Therefore, it is necessary to take different actions to enhance the mass transport. A detailed discussion of charge is provided in the SI.

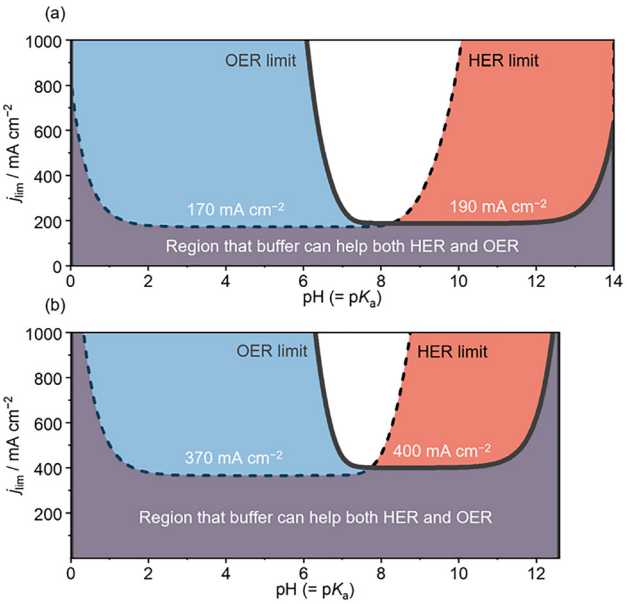

Fig. 5 Summary of limiting current density in 3 M K-buffer (HA^-/A^{2-}) solutions. The solid line is the limiting current of water oxidation supported by buffer species, and the dashed line is the limiting current of direct reduction of buffer species. The results of the HER are from Fig. S13 and the results of the OER are the same as those in Fig. 4. (a) 25 °C. (b) 80 °C.

One of the ways to increase the mass transport of species is the convection, which is the rotation speed of the RDE in this study. Fig. S16(a) describes the enhancement of the $j_{\text{lim-OH oxi.}}$ in 3 M buffer solutions at pH = pK_a = 10. The $j_{\text{lim-OH oxi.}}$ is 400 mA cm^{-2} under static conditions at 80 °C, surpassing 1 A cm^{-2} at 1000 rpm, which is a reasonable applied rotation speed for RDE experiments. The fluid velocities at the surface are shown in Fig. S16(b). At 50 μm, the fluid velocity on RDE rotating at 1000 rpm becomes 24 times as fast as that at 100 rpm. These results highlight the importance of convection and accelerating the fluid flow in flow cells for industrialization.

In conclusion, Fig. 6 summarizes how optimization of electrolyte conditions increases $j_{\text{lim-OH oxi.}}$. In unbuffered solutions, the obtainable current density is below 0.1 mA cm^{-2} under non-extreme pH conditions, which causes a large pH shift at the surface. Adding buffer species can enhance the limiting current, while concentration and temperature need to be increased. To meet the industrial demand, electrolyte flow also has a significant impact. Therefore, further studies on the electrolyte flow in the commercialized flow cell and how it can be connected to the RDE configuration are essential. In the flow cell, the porous separator divides the anode and cathode, thus

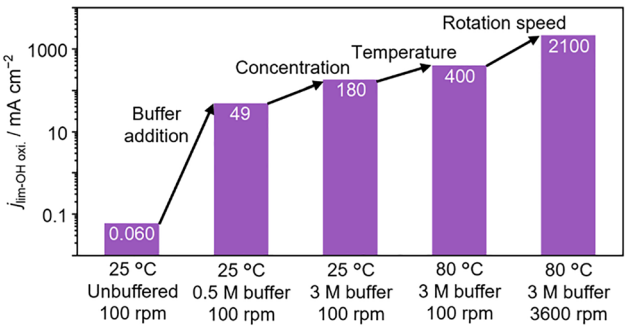

Fig. 6 Summary of how electrolyte engineering increases $j_{lim\text{-}OH\ oxi.}$ in solutions at pH 10. Non-buffer solutions: 0.1 M $KClO_4$ + KOH. Buffer solutions: pH = pK_a = 10. The potential of Ni RDE was assumed to be 1.5 V *vs.* RHE. Properties such as electrolyte viscosity, density, diffusion coefficients, and ion sizes were taken from *x* M K-carbonate solutions at that temperature.

the mass transport among the separator is also influential. Furthermore, this study neglected bubble-induced convection, which is known to help to minimize the local pH shift.[51] Particularly at high current density, lots of bubbles are produced at electrodes, enhancing the fluid flow close to the electrodes. Conducting multiphase fluid dynamics will lead to further understanding of the fluid flow impact toward the mass transport of species. Nevertheless, this study highlighted the importance of electrolyte engineering in consideration of overall water splitting.

Conclusions

This study provides a quantitative framework for understanding the mass-transport limitations of buffer electrolytes in water electrolysis under non-extreme pH conditions. By numerically resolving ion transport using the GMPNP equations, we elucidate how electrolyte composition and operating conditions govern the attainable limiting current densities for both the HER and OER. While acid–base equilibria, reflected by buffer pK_a and water pK_w, influence the individual half-reactions, our analysis reveals that diffusion of buffer species becomes the dominant constraint when the HER and OER are considered together in a full electrolysis system. Importantly, increasing buffer concentration and temperature, in combination with enhanced electrolyte convection, effectively overcomes these transport limitations and enables current densities relevant to industrial operation. These results provide quantitative guidance on electrolyte composition and operating conditions, and establish electrolyte engineering—through deliberate control of buffer chemistry and mass transport—as a viable strategy for realizing high-performance water electrolysis using buffer-based electrolytes under non-extreme pH conditions.

Author contributions

MW: data curation, investigation, visualization, writing – original draft. KO: conceptualization, supervision, writing – review & editing. KT: conceptualization, funding acquisition, supervision, writing – review & editing.

Conflicts of interest

There are no conflicts to declare.

Data availability

Data for this article are available at ZENODO at https://doi.org/10.5281/zenodo.18797932.

Supplementary information (SI) is available. See DOI: https://doi.org/10.1039/d6ey00006a.[52–58]

Acknowledgements

This work was supported financially by the GteX Program Japan (Grant Number JPMJGX23H2) and the MEXT Program: Data Creation and Utilization-Type Material Research and Development Project (Grant Number JPMXP1122712807).

References

1 K. T. Møller, T. R. Jensen, E. Akiba and H. Li, *Prog. Nat. Sci.: Mater. Int.*, 2017, **27**, 34.
2 IRENA, *Making the breakthrough: Green Hydrogen policies and technology costs*, International Renewable Energy Agency, Abu Dhabi, 2021.
3 S. S. Jeon, W. Lee, H. S. Jeon and H. Lee, *ChemSusChem*, 2024, **17**, e202301827.
4 J. Wang, J. Wen, J. Wang, B. Yang and L. Jiang, *Renewable Sustainable Energy Rev.*, 2024, **203**, 114779.
5 M. F. Lagadec and A. Grimaud, *Nat. Mater.*, 2020, **19**, 1140.
6 D. M. See and R. E. White, *J. Chem. Eng. Data*, 1997, **42**, 1266.
7 A. Bergmann, I. Zaharieva, H. Dau and P. Strasser, *Energy Environ. Sci.*, 2013, **6**, 2745.
8 M. W. Kanan and D. G. Nocera, *Science*, 2008, **321**, 1072–1075.
9 P. M. Zhang, M. Wang, H. Chen, Y. Liang, J. Sun and L. Sun, *Adv. Energy Mater.*, 2016, **6**, 152319.
10 D. G. Nocera, *Inorg. Chem.*, 2009, **48**, 10001.
11 T. Shinagawa and K. Takanabe, *J. Phys. Chem. C*, 2015, **119**, 20453.
12 T. Shinagawa and K. Takanabe, *J. Phys. Chem. C*, 2016, **120**, 24187.
13 T. Shinagawa, M. T. Ng and K. Takanabe, *ChemSusChem*, 2017, **10**, 4155.
14 T. Nishimoto, T. Shinagawa, T. K. Naito and K. Takanabe, *ChemSusChem*, 2021, **14**, 1554.
15 K. Obata, L. Stegenburga and K. Takanabe, *J. Phys. Chem. C*, 2019, **123**, 21554.
16 J. Durst, A. Siebel, C. Simon, F. Hasché, J. Herranz and H. A. Gasteiger, *Energy Environ. Sci.*, 2014, **7**, 2255.

17 W. Sheng, H. A. Gasteiger and Y. Shao-Horn, *J. Electrochem. Soc.*, 2010, **157**, B1529.
18 T. Shinagawa and K. Takanabe, *ChemSusChem*, 2017, **10**, 1318.
19 I. Katsounaros, J. C. Meier, S. O. Klemm, A. A. Topalov, P. U. Biedermann, M. Auinger and K. J. J. Mayrhofer, *Electrochem. Commun.*, 2011, **13**, 634.
20 M. Auinger, I. Katsounaros, J. C. Meier, S. O. Klemm, P. U. Biedermann, A. A. Topalov, M. Rohwerder and K. J. J. Mayrhofer, *Phys. Chem. Chem. Phys.*, 2011, **13**, 16384.
21 T. Shinagawa, K. Obata and K. Takanabe, *ChemCatChem*, 2019, **11**, 5961.
22 G. Marcandalli, K. Boterman and M. T. M. Koper, *J. Catal.*, 2021, **405**, 346.
23 C. Hu, L. Zhang and J. Gong, *Energy Environ. Sci.*, 2019, **12**, 2620.
24 X. Xie, L. Du, L. Yan, S. Park, Y. Qiu, J. Sokolowski, W. Wang and Y. Shao, *Adv. Funct. Mater.*, 2022, **32**, 2110036.
25 T. Naito, T. Shinagawa, T. Nishimoto and K. Takanabe, *Inorg. Chem. Front.*, 2021, **8**, 2900.
26 L. Giordano, B. Han, M. Risch, W. T. Hong, R. R. Rao, K. A. Stoerzinger and Y. Shao-Horn, *Catal. Today*, 2015, **262**, 2.
27 J. Rossmeisl, A. Logadottir and J. K. Nørskov, *Chem. Phys.*, 2005, **319**, 178.
28 T. Nishimoto, T. Shinagawa, T. Naito and K. Takanabe, *J. Catal.*, 2020, **391**, 435.
29 Z. Zhou, Z. Pei, L. Wei, S. Zhao, X. Jian and Y. Chen, *Energy Environ. Sci.*, 2020, **13**, 3185.
30 A. J. Bard and L. R. Faulkner, *Electrochemical Methods Fundamentals and Applications*, John Wiley & Sons, Inc., 2001.
31 T. Naito, T. Shinagawa, T. K. Nishimoto and K. Takanabe, *ChemSusChem*, 2020, **13**, 5921.
32 P. W. Atkins and J. de Paula, *Atkins' Physical Chemistry*, 10 edn, Freeman and Company, New York, 2014.
33 D. Bohra, J. H. Chaudhry, T. Burdyny, E. A. Pidko and W. A. Smith, *Energy Environ. Sci.*, 2019, **12**, 3380.
34 H. Wang, A. Thiele and L. Pilon, *J. Phys. Chem. C*, 2013, **117**, 18286.
35 E. F. Johnson, E. Boutin, S. Liu and S. Haussener, *EES Catal.*, 2023, **1**, 704.
36 J. Gu, S. Liu, W. Ni, W. Ren, S. Haussener and X. Hu, *Nat. Catal.*, 2022, **5**, 268.
37 E. F. Johnson, E. Boutin and S. Haussener, *J. Phys. Chem. C*, 2023, **127**, 18784.
38 D. R. Lide, L. I. Berger, R. N. Goldberg, H. V. Kehiaian, K. Kuchitsu, D. L. Roth and D. Zwillinger, *CRC Handbook of Chemistry and Physics*, 87th edn, Taylor and Francis, Boca Raton, 2006.
39 T. Burdyny, P. J. Graham, Y. Pang, C. Dinh, M. Liu, E. H. Sargent and D. Sinton, *ACS Sustainable Chem. Eng.*, 2017, **5**, 4031.
40 K. G. Schulz, U. Riebesell, B. Rost, S. Thoms and R. E. Zeebe, *Mar. Chem.*, 2006, **100**, 53.
41 G. Valette, *J. Electroanal. Chem.*, 1981, **122**, 285–297.
42 D. C. Grahame, *Chem. Rev.*, 1947, **41**, 441.
43 P. Xu, A. D. Von Rueden, R. Schimmenti, M. Mavrikakis and J. Suntivich, *Nat. Mater.*, 2023, **22**, 503.
44 T. Shinagawa, A. T. Garcia-esparza and K. Takanabe, *Chem-ElectroChem*, 2014, **1**, 1497.
45 L. J. J. Janssen and J. G. Hoogland, *Electrochim. Acta*, 1970, **15**, 1013.
46 M. Jamesh and X. Sun, *J. Power Sources*, 2018, **400**, 31.
47 H. Komiya, K. Obata, M. Wada, T. Nishimoto and K. Takanabe, *ACS Sustainable Chem. Eng.*, 2023, **11**, 12614.
48 M. Wada, K. Obata, V. Agarwal, F. Lorenzutti, S. Haussener and K. Takanabe, *ACS Electrochem.*, 2025, **1**, 2521.
49 X. Huang, J. Xu, J. Gao, Y. Cui, X. Xu and S. Wang, *J. Phys. Chem. C*, 2024, **128**, 11278.
50 X. Huang, J. Xu, X. Xu and S. Wang, *ACS Catal.*, 2024, **14**, 14606.
51 K. Obata and F. F. Abdi, *Sustainable Energy Fuels*, 2021, **5**, 3791.
52 J. J. López-García, J. Horno and C. Grosse, Poisson–Boltzmann Description of the Electrical Double Layer Including Ion Size Effects, *Langmuir*, 2011, **27**, 13970–13974.
53 J. Newman and K. E. T. Alyea, *Electrochemical Systems* 3rd edn, John Wiley & Sons, Inc., Hoboken, New Jersey, 2004.
54 R. Kas, K. Yang, G. P. Yewale, A. Crow, T. Burdyny and W. A. Smith, *Ind. Eng. Chem. Res.*, 2022, **61**, 10461.
55 E. R. Nightingale, *J. Phys. Chem.*, 1959, **63**, 1381.
56 R. D. Shannon, *Acta Cryst.*, 1976, **A32**, 751.
57 H. D. B. Jenkins and K. P. Thakur, *J. Chem. Educ.*, 1979, **56**, 576.
58 H. K. Roobottom, H. D. B. Jenkins, J. Passmore and L. Glasser, *J. Chem. Educ.*, 1999, **76**, 1570.